RPE | Radiation Physics & Engineering
A Peer-Reviewed Journal
Published by K.N. Toosi University of Technology
http://rpe.kntu.ac.ir
Research Article

Radiation Physics and Engineering 2026; ?(?):?–?

Proton therapy enhancement with gold, platinum, and iridium nanoparticle: A cellular-scale Geant4-DNA study

Fatemeh Habibi[a], Zohreh Parang[a,*], Nasrin Hoseini-Motlagh[a], Alireza Keshavarz[b]

[a] *Department of Physics, Shi. C., Islamic Azad University, Shiraz, Iran*
[b] *Department of Physics, Shiraz University of Technology, Shiraz, Iran*

HIGHLIGHTS

- Various NPs were investigated for microscopic dose enhancement in proton therapy.
- Higher DNA damages were induced at the end of the SOBP than its center.
- Ir and Pt NPs have superiority over Au in proton dose enhancement.
- Ir and Pt are promising radio-sensitizers for 62.8 MeV proton therapy.

ABSTRACT

Combining nanoparticles (NPs) with proton therapy holds promise for improving treatment gain. Prior simulation studies often lack clinical beam realism and comprehensive radiobiological endpoints, leading to conflicting results. This study employs a Geant4-DNA Monte Carlo simulation to compare the physical and radiobiological enhancement of Au, Pt, and Ir NPs in a human cell under a clinically relevant Spread-Out Bragg Peak proton beam. A 62.8 MeV SOBP was simulated, then, phase-space files at the beam's entrance, plateau, and distal edge were obtained. They used to irradiate a fibroblast cell containing 30 mg.g^{-1} NPs in the cytoplasm. Three NP sizes of 10, 50, and 100 nm were investigated at each phase-space. We calculated the dose enhancement factor (DEF) and total DNA damage enhancement. Furthermore, cell survival curves were predicted using the Two-Lesion Kinetic model. The results indicated that Ir NPs yielded the highest physical dose enhancement (up to 4.21% for 10 nm size), followed by Pt NPs (up to 4.10%). Smaller NPs tend to present a higher DEF than larger NPs. DNA damage yields increased with linear energy transfer (LET), with the distal SOBP distal edge showing the greatest enhancement. Cell survival curves indicated a detectable reduction in survival fraction for Ir > Pt > Au NPs at the distal edge, correlating with increased complex DNA damage. Under clinically realistic simulation conditions, high atomic number and high density NPs like Ir provide a modest but consistent physical and radiobiological enhancement in proton therapy, most pronounced at the high-LET Bragg peak.

KEYWORDS

Proton therapy
Dose enhancement factor
Nanoparticles
DNA damage
Radiobiology
Geant4-DNA

HISTORY

Received: 15 February 2026
Revised: 5 May 2026
Accepted: 16 May 2026
Published: In Press

1 Introduction

Proton therapy is a treatment modality for certain common cancers -including those of the eye, brain, and lung- that has shown promising clinical outcomes, although its use remains limited globally (Mohan, 2022). Protons offer unique advantages as a radiation source in oncology. Upon entering tissue, protons deposit relatively low energy along the initial part of their path, but release the majority of their energy at a precise depth near the end of their range. This phenomenon, known as the Bragg peak, results in a sharp dose maximum at the tumor site, as illustrated by plotting dose deposition against depth (Newhauser and Zhang, 2015). This enables the delivery of a maximal radiation dose to the tumor while sparing adjacent healthy tissues and organs -a significant advantage over conventional X-ray and gamma radiation therapies.

Recent research has explored the use of gold nanoparticles (Au NPs) to further enhance radiation dose within tumors (Hainfeld et al., 2008; Rudek et al., 2019; Cunningham et al., 2021). However, findings regarding the magnitude of this enhancement in proton therapy have

*Corresponding author: parang@iau.ac.ir

https://doi.org/10.22034/rpe.2026.575951.1345

been mixed. In an in vitro study by Smith et al. (Smith et al., 2017), the dose enhancement from Au NPs under a spread-out Bragg peak (SOBP) generated by 150 MeV protons was found to be less than 5%, a value within experimental uncertainty. In contrast, Sisin et al. (Sisin et al., 2022) reported a measurable dose enhancement of approximately 9% (±3%) under similar irradiation conditions using EBT3 radiochromic films for dosimetry.

Radiobiological research in proton therapy is primarily focused on key endpoints, including the determination of relative biological effectiveness (RBE) across a spectrum of linear energy transfer (LET) values. A major objective is also to quantify proton-induced DNA double-strand breaks (DSBs) and apply these data to model cellular repair mechanisms, ultimately enabling the prediction of cell survival curves. From a radiobiological perspective, growing evidence suggests that proton therapy could be rendered more effective when gold nanoparticles (Au NPs) are present within the tumor, as highlighted in studies by Polf et al. (Polf et al., 2011), Hojo et al. (Hojo et al., 2017), Li et al. (Li et al., 2019), Torrisi et al. (Torrisi et al., 2020), and Velten and Tome (Velten and Tomé, 2023).

Given practical constraints such as limited laboratory resources and restricted access to proton therapy facilities, Monte Carlo simulations have become an indispensable tool for researchers and physicists, supporting both dosimetry calculations and treatment planning. A substantial body of simulation-based research has examined the dose enhancement effects of gold nanoparticles (Au NPs) in proton therapy. These studies span multiple scales: macroscopic approaches focus on tumor-level effects, while microscopic investigations explore cellular and DNA-level interactions (Martínez-Rovira and Prezado, 2015; McNamara et al., 2016; Sotiropoulos et al., 2017; Peukert et al., 2020; Huynh and Chow, 2021; Rajabpour et al., 2022; Mansouri et al., 2024; Alamgir et al., 2025). For instance, Heuskin et al. (Heuskin et al., 2017) demonstrated that low-energy protons (approximately 1.3 MeV) can generate up to 32% more secondary electrons in the vicinity of a single Au NP compared to scenarios without the nanoparticle. However, no significant dose enhancement was observed in a mammalian cell model incorporating a large number of Au NPs. Additional studies have explored how the diameter and spatial distribution of Au NPs influence the dose enhancement factor (DEF) in proton therapy (Lin et al., 2015; Peukert et al., 2020). More recently, research has expanded beyond gold to investigate other types of NPs for potential application in proton therapy. These include superparamagnetic iron oxide (Fe_3O_4), boron-11 (B-11), carbon (C), platinum (Pt), silver (Ag), and bismuth (Bi) nanoparticles (Ahn et al., 2018; Tabbakh et al., 2022; Tabbakh and Hosmane, 2023; Zavestovskaya et al., 2023, 2024).

Although interesting simulation studies have been carried out so far, there is an obvious discrepancy in some results, which is due to the difference in the distribution of Au NPs. On the other hand, the way to define the proton beam is also important, which is defined differently in the relevant articles. In many articles, the proton beam is defined without an accelerator as a mono-energetic radiation source, which is different from the clinical situation where an SOBP is used to cover the entire tumor. For Monte Carlo simulations at the microscopic scale, the definition of the radiation source has been observed as the usual way (i.e., primary protons) and as a phase-space (PS) (i.e., the emission of secondary particles at certain points of the proton range specifically at the Bragg peak location). A key limitation in some previous simulations was the confinement of primary proton transport to a single nanoparticle. In these models, protons were effectively forced to originate on one surface of the NP and terminate on the opposite side, artificially guaranteeing an interaction. This type of source definition seems to suffer from a lack of equilibrium of charged particles. Therefore, the DEF values obtained around the NP, which are sometimes reported up to 16, cannot be very accurate and may not be generalized to the whole cell. A better method is to simulate a cell nucleus and consider NPs in large numbers, which has the advantage of considering a specific mass concentration for NPs (in $mg.g^{-1}$ or ppm). This is closer to real conditions.

Multiscale Monte Carlo simulations gained a lot of interest in numerous studies (Klapproth et al., 2021; Martinov et al., 2023a,b; Ahmadi Ganjeh and Mosleh-Shirazi, 2024). Since there is a lack of data comparing these different simulation models in the literature, the present study aims to calculate the microscopic DEF for an SOBP therapeutic beam (62.8 MeV) as a multiscale Monte Carlo simulation. A 62.8-MeV proton beam was chosen because it is a common therapeutic energy for the treatment of ocular tumors (Jia et al., 2016). At the macroscopic stage, three PS files were defined in the beginning, middle, and end of the SOBP. The information of the produced secondary particles along with the primary protons were stored in each PS. These particles were used as the primary radiation source in the microscopic stage. At the microscopic stage, after defining a fibroblast mammalian cell, various NPs (Au, Pt, and Ir) with different sizes (10, 50, and 100 nm) and a fixed concentration of 30 $mg.g^{-1}$ were randomly implanted in the cytoplasm of the cell (see Sotiropoulos et al., (Sotiropoulos et al., 2017)).

Beyond calculating the DEF, we quantified and compared the DNA damage induced by each NP. To link this physical damage to the ultimate biological outcome, cancer cell death, we employed a mathematical survival and repair model within Geant4-DNA to generate cell survival curves for SOBP irradiation, both with and without the presence of Au, Pt, and Ir NPs with different sizes of 10, 50, and 100 nm.

The specific innovations of this work are threefold: 1- Conducting a comparison of high-atomic number NPs such as Au, Pt, and Ir NPs under identical, controlled conditions. This allows for a direct ranking of their intrinsic physical radio-enhancing potential, providing valuable data for material selection beyond the commonly studied Au. 2- Employing a SOBP beam of 62.8 MeV protons, generated using a validated model of a clinical passive scattering system, rather than a simplified mono-energetic source. 3- Quantify the induced DNA damage spectra and, crucially, translate these into predictions of cell sur-

vival probability. This provides a direct link between the physical presence of nanoparticles and their potential ultimate biological effect, a step rarely taken in multiscale NP-proton simulation studies.

2 Materials and Methods

2.1 Simulation Code, Physics and Chemistry

For this study, simulations were conducted using the Geant4 Monte Carlo toolkit (version 11.1.3; Agostinelli et al., (Agostinelli et al., 2003)). At the macroscopic stage of the investigation, the phase-space (PS) file was generated using the Geant4 toolkit. The QGSP_BIC reference physics list was selected due to its widespread validation and application in proton and hadron therapy simulations (Cirrone et al., 2005; Allison et al., 2016). This physics list integrates multiple physics components, including models for hadronic elastic and inelastic interactions (via G4HadronElasticPhysics and G4HadronPhysicsQGSP_BIC), standard electromagnetic processes (G4EmStandardPhysics), particle decay processes (G4DecayPhysics), as well as additional modules for ion interactions, neutron transport, and tracking cuts (e.g., G4IonPhysics, G4NeutronTrackingCut). A comprehensive overview of reference physics lists can be found in the Geant4 Collaboration guide (Geant4 Collaboration, 2023).

For the microscopic calculation of the dose enhancement factor (DEF) at the cellular scale, the Geant4-DNA extension was employed (Incerti et al., 2010a). This extension utilizes a track-structure algorithm, offering high-precision simulations at the microscopic level. It provides dedicated track-structure physics models for electrons (up to 1 MeV) and protons (up to 300 MeV) in liquid water. The G4EmDNAPhysics_option4 physics constructor was specifically chosen due to its suitability for simulating DNA damage. Production thresholds for secondary particles were set at 1 μm for the macroscopic phantom and 0.001 μm for the cellular geometry. Additionally, Geant4-DNA supports the simulation of the chemical stage, enabling the modeling of radical formation, diffusion, and reactions resulting from water radiolysis (Karamitros et al., 2011, 2014). Detailed information on the physics models and their applicable energy ranges can be found in the relevant literature (Incerti et al., 2010b, 2018; Kyriakou et al., 2021).

To simulate the pre-chemical and chemical stages in this work, the updated "G4EmDNAChemistry_option3" chemistry constructor from Geant4-DNA version 11.1 was utilized. This constructor employs the synchronous Independent Reaction Times (IRT) algorithm, which models the diffusion and interactions of key radiolytic species through predefined reaction radii and rates (Tran et al., 2021). This chemistry module enabled us to assess indirect DNA damage resulting from hydroxyl radicals produced during water radiolysis, with comparisons made between nanoparticle-present and nanoparticle-absent conditions. The chemical stage was simulated over a duration of 2.5 ns, in accordance with the time frame established by Meylan et al. (Meylan et al., 2017). Comprehensive descriptions of the IRT algorithm are available in the works of Plante and Devroye (Plante and Devroye, 2017), Ramos-Mendez et al. (Ramos-Méndez et al., 2020), and Tran et al. (Tran et al., 2021).

2.2 Cell Modelling and NPs

The cell geometry is defined using the "molecularDNA" example (Chatzipapas et al., 2023) of the Geant4 Monte Carlo toolkit. The geometry is constructed using a Hilbert curve, a continuous fractal space-filling algorithm (Hilbert, 1935). This fractal design enables the dense, non-overlapping packing of a repeating DNA segment in three dimensions. The complete chromatin fiber is assembled from three fundamental voxel types representing distinct DNA configurations: straight, turned, and turned with a 90° twist, each incorporating histone proteins. The smallest part of DNA is a base pair (bp) or a nucleotide pair. Six spheres were modeled as DNA molecules, and they were assembled to construct a nucleotide pair: 2 bases, 2 phosphates, and 2 sugars. Each nucleotide consists of three volumes: 2-deoxyribose, phosphoric acid, and the bases: Adenine ($C_5H_5N_5$), Thymine ($C_5H_6N_2O_2$), Cytosine ($C_4H_5N_3O$), and Guanine ($C_5H_5N_5O$). The histone protein is a cylinder with a radius of 3.75 nm and a height of 5.75 nm. A nucleosome is formed by a histone core wrapped by 216 bp of DNA. The total modeled chromatin fiber has a length of 6.4 Gbp, confined within an ellipsoidal nuclear volume of dimensions $14.2 \times 5.0 \times 14.2$ μm^3 via a geometric mask, resulting in an effective DNA density of $\sim$0.015 bp.nm^{-3}. The hierarchical geometric details are documented in prior works (Sakata et al., 2019; Shin et al., 2021). For a schematic visualization of the cell nucleus, please refer to our previous study (Habibi et al., 2025).

To define NPs in the cell, an ellipsoid shell of water with a thickness of 1 μm was defined as the cytoplasm around the cell nucleus. Thus, the whole cell has $15.2 \times 6.0 \times 15.2$ μm3 dimensions (See Fig. 3). Au, Pt, and Ir NPs with a diameter of 10, 50, and 100 nm with a concentration of 30 mg.g^{-1} (i.e., 3% weight percentage) were randomly distributed in the cytoplasm. The possible overlapping of NPs was eliminated using Geant4's G4ThreeVector and a rejection-sampling algorithm to ensure spatial randomness. The number of NPs was a direct computational result of applying the fixed parameters: cell cytoplasm volume, nanoparticle size (10 or 50 or 100 nm), material density, and the target mass concentration (30 mg.g^{-1}). The number of NPs for each material is calculated by Eq. (1):

$$\text{NP number} = \frac{C \times Cell_{volume} \times Cell_{density}}{NP_{volume} \times NP_{density}} \quad (1)$$

where C is the concentration of NPs in percentage. Due to the different densities of NP's materials, the number of NPs required for the concentration of 30 mg.g^{-1} was also different (see Table 1).

We acknowledge that 30 mg.g^{-1} is a therapeutic concentration, representing an upper-bound or "best-case" physical scenario. It is used to establish the maximum

Table 1: The total number of nanoparticles (of 50 nm diameter) in the cell according to the concentration of 30 mg.g^{-1} (3%).

NP material	Size (nm)	Density (g.cm^{-3})	Cell volume (cm^3)	NP volume (cm^3)	Total number of NP
Au	10	19.32	6.54E-26	7.26E-19	2,152,547
	50				17,221
	100				2,153
Pt	10	22.45	6.54E-26	7.26E-19	1,938,798
	50				15,547
	100				1,939
Ir	10	22.56	6.54E-26	7.26E-19	1,843,404
	50				14,478
	100				1,844

theoretical dose enhancement achievable by each material's physical properties. This is a common and valuable approach in computational physics to rank materials before costly and complex biological experiments. If a biologically typical low concentration (e.g., 0.1-1 mg.g^{-1}) were used, the resulting DEF and DNA damage differences might be smaller than the statistical uncertainty of our Monte Carlo simulation, making a material-by-material comparison inconclusive.

2.3 Radiation Source

The SOBP was generated using the Geant4 'Hadrontherapy' advanced example (Cirrone et al., 2005, 2011), which models clinical proton and carbon ion beamlines. Based on our previous study (Habibi et al., 2025), we simulated a 62.8-MeV passive scattering proton beamline modeled after the ocular therapy facility at Laboratori Nazionali del Sud (INFN), Italy (Cirrone et al., 2011). Protons with an initial energy of 62.8 MeV were directed as a 2 mm radius beam into a $25 \times 25 \times 25$ cm^3 liquid water phantom. A ∼10 mm SOBP was created in the phantom using the example's built-in range modulator wheel, which superimposes 12 weighted pristine Bragg peaks. The corresponding modulator thicknesses and relative weights are provided in our previous study (Habibi et al., 2025), consisted with the study of Jia et al., (Jia et al., 2016). The resulting depth-dose profile is shown in Fig. 1. Phase-space (PS) files were recorded at three depths, entrance (0.5 mm), plateau (26.5 mm), and distal edge (31.5 mm), using virtual detectors ($25 \times 25 \times 0.1$ cm^3) placed at these positions.

The PS file recorded the type and energy of all primary and secondary particles intersecting the virtual detector. This file subsequently served as the radiation source for the microscopic cell irradiation. At the cellular scale, particles were sampled from the PS and emitted from a circular plane (7.6 μm radius) positioned to fully encompass the cell nucleus and cytoplasm, ensuring complete cell coverage (Fig. 2).

A 62.8 MeV proton beam was selected because it is clinically used for ocular proton therapy at several facilities. While higher energies (up to 250 MeV) are used for deep-seated tumors, the physical mechanism of NP-enhanced dose enhancement depends primarily on LET, not absolute energy. Our LET-dependent findings (comparing PS1-PS3) are therefore qualitatively generalizable to the Bragg peak region of higher-energy SOBPs. The 62.8 MeV beam also allowed efficient use of computational resources for cellular-scale simulations.

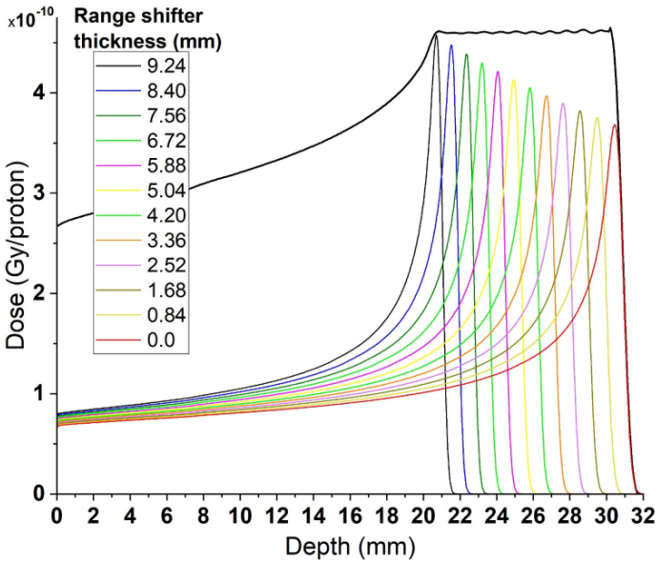

Figure 1: The SOBP obtained using the Geant4 "Hadrontherapy" example with a 62.8 MeV proton beam in a passive transport beam line. The locations of obtaining the phase-space (PS) are indicated by three dashed lines at depths of 0.5 mm (at the beginning), 26.5 mm (at the middle) and 31.5 mm (at the end).

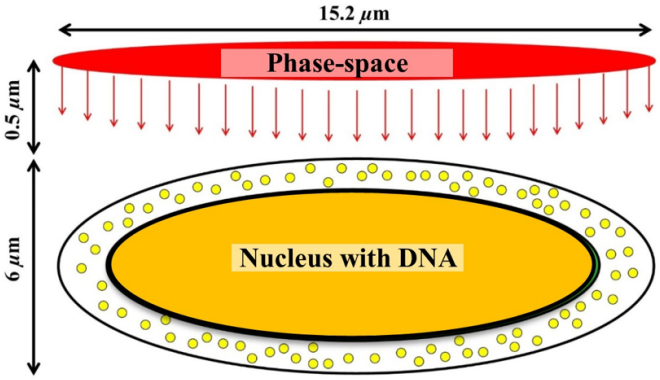

Figure 2: The cell model irradiating by a circular plane source with a radius of 7.6 μm emitting particles from a phase-space file.

2.4 DEF and DNA Damage Calculation

To evaluate the dose enhancement, the DEF is defined as the ratio of the dose deposited in a cell containing nanoparticles in its cytoplasm (D_{NP}) to that in a cell without nanoparticles (D_0), as expressed in Eq. (2):

$$DEF = \frac{D_{NP}}{D_0} \tag{2}$$

DNA damage is broadly divided into two categories: single-strand breaks (SSBs) and double-strand breaks (DSBs). Damage may further arise from direct effects of radiation, indirect effects mediated by free radicals, or a combination of both, referred to as hybrid damage (Mortazavi et al., 2024). Complex DSBs (the proximity of multiple DSBs close together) are particularly important for modeling cellular repair processes and predicting cell survival outcomes.

An SSB was scored if an energy deposition of at least 5 eV occurred within a sugar-phosphate group of the DNA backbone. This value represents the minimum energy threshold for break induction, with the probability of an SSB increasing linearly with deposited energy up to a maximum of 37.5 eV, at which point the break is considered certain. The maximum energy threshold for the SSB occurrence is 37.5 eV, which means the probability of an SSB will be 100% when an energy deposition of 37.5 eV or greater occurs in the backbone of the DNA (Francis et al., 2011). Two SSBs located on opposite DNA strands with a distance of less than ∼3.4 nm (or 10 bps) lead to a DSB. To consider the quasi-direct effect, a radial distance of 0.6 nm beyond each sugar-phosphate molecule was determined as hydration shells. This effect refers to the damage caused by charge transfers following ionization of the hydration shell around the DNA molecules (Bertolet et al., 2022). In the case of indirect DNA damages, the presence of the chemical species in the sugar-phosphate molecules may lead to SSB. Only hydroxyl radical (OH•) was taken into account for calculating indirect DNA damage, since it is the most reactive radical. Note that only a fraction of OH• that reach the DNA backbone were assumed to cause a break. Based on established parameters, a 40% probability was assigned for an OH• radical interacting with a sugar-phosphate site to induce an indirect SSB (Lampe et al., 2018; Sakata et al., 2019; Chatzipapas et al., 2023). Chemical species diffusing beyond 4 nm from the DNA were terminated, consistent with the estimated effective radical diffusion range for inducing DNA damage (Nikjoo et al., 1997). All simulations were performed on a 64-core computing system with 192 GB of RAM. Statistical uncertainties in the macroscopic dose were maintained below 1% by simulating 2×10^6, 1×10^6, and 5×10^5 primary particles for the PS1, PS2, and PS3 phase-space files, respectively.

2.5 Statistical uncertainty

The Mersenne Twister engine (MTwistEngine) was used as the random number generator. For each unique simulation condition (NP type, phase-space location), three independent runs were performed. Each run was initialized with a distinct, non-repeating seed derived from the system clock to ensure statistical independence. The mean and standard error of the mean across these three runs were calculated for all reported quantities (dose, DNA damage yields). This protocol ensures the reproducibility of our averaged results while accounting for run-to-run stochastic variation.

The statistical uncertainty on absorbed dose was calculated using the history-by-history method implemented in Geant4, which provides a reliable estimate of the relative standard error. A minimum of 510 primary particles (for PS3) was used to ensure this uncertainty was <1% at the macroscopic stage and <0.2% in the cellular scoring volumes.

2.6 Cell Survival Calculation

Ionizing radiation induces a yield of DNA damage that accumulates during irradiation, a portion of which is subsequently repaired over time. To translate this simulated damage into a biological endpoint, the cell survival fraction (SF) was calculated using the publicly available Python modules from the Geant4 "molecularDNA" example. This framework incorporates two established radiobiological models: The Two-Lesion Kinetic (TLK) model and the Local Effect Model (LEM). We selected the TLK model (Stewart, 2001) for this study. The TLK formalism links DNA double-strand breaks (DSBs) to cell death by categorizing DSBs based on their complexity. Simple, isolated DSBs are considered repairable, while complex lesions are treated as potentially lethal. The model incorporates two repair kinetics: a fast, first-order process for the correct rejoining of simple breaks, and a slow, second-order process that accounts for the misrepair of complex lesions, which can lead to fatal chromosomal aberrations. These processes are mathematically represented by the time-dependent parameters $L(t)$ and $L^2(t)$, respectively. To calculate the cell SF, the TLK model introduces the Eqs. (3) to (5) (Chatzipapas et al., 2023):

$$\frac{dL_1(t)}{dt} = \dot{D}(t) Y \Sigma_1 - \lambda_1 L_1(t) - \eta L_1[L_1(t) + L_2(t)] \tag{3}$$

$$\frac{dL_2(t)}{dt} = \dot{D}(t) Y \Sigma_2 - \lambda_2 L_2(t) - \eta L_2[L_1(t) + L_2(t)] \tag{4}$$

$$\frac{dL_f(t)}{dt} = \beta_1 \lambda_1 L_1(t) + \beta_2 \lambda_2 L_2(t) + \gamma\, \eta [L_1(t) + L_2(t)]^2 \tag{5}$$

where $L_1(t)$ and $L_2(t)$ represent the time-dependent yields (per cell) of simple and complex DSBs, respectively. These correspond to lesions undergoing fast and slow repair kinetics. $L_f(t)$ denotes the accumulated yield of lethal (unrepaired or misrepaired) damage. The genome length Y (in Gbp) and the dose rate $\dot{D}(t)$ scale the damage induction. The initial yields of simple (Σ_1) and complex (Σ_2) DSBs are input parameters derived from the simulations, accounting for the greater severity of clustered breaks (Sakata et al., 2020; Chatzipapas et al., 2023).

Within the TLK model formalism, the induced DNA damages are categorized as follows for input into Eqs. (2) to (4) simple DSBs (isolated DSBs) are treated as repairable lesions (L_1), while complex lesions are pooled as

irreparable/lethal lesions (L_2) with a higher probability of leading to cell death. In the TLK model, simple lesions undergo fast repair, while complex lesions are processed by a slow repair pathway. The repair kinetics are governed by rate parameters: λ_1 and λ_2 (h^{-1}) for the first-order repair of simple and complex lesions, respectively, and η (h^{-1}) for the second-order misrepair interaction. The probability that residual damage leads to cell death is defined by lethality coefficients: β_1 and β_2 for simple and complex lesions, and γ for misrepaired pairs. All parameter values were adopted for a fibroblast cell nucleus from Chatzipapas et al. (Chatzipapas et al., 2023). The system of differential equations (Eqs. (3) to (5)) was solved numerically using a fourth-order Runge-Kutta algorithm as implemented in the "molecularDNA" Python scripts. The resulting lethal damage yield L_f was then used to calculate the SF via Eq. (6).

$$SF = e^{-L_f} \tag{6}$$

Table 2 summarizes the TLK parameters according to Chatzipapas et al., (Chatzipapas et al., 2023).

The TLK model was selected over alternative survival models because it provides a direct mechanistic link between the DSB complexity spectrum derived from our simulations (simple vs. complex DSBs) and cell death. The model is natively implemented in the Geant4-DNA molecularDNA example, ensuring reproducibility and consistency with our simulation workflow. While newer models exist, the TLK model's parameters for fibroblast cells are well-established, and its mechanistic foundation aligns with our goal of connecting physical damage patterns to biological outcome.

3 Results

For validating the simulation, the simulated Bragg peak depth-dose curve for 62.8 MeV protons in water was compared against experimental ionization chamber data supplied with the Geant4 'Hadrontherapy' example (Cirrone et al., 2005, 2011). As shown in Fig. 3, the simulation exhibits excellent agreement with the reference measurements.

Table 2: Simulation parameters for generating cell survival curves by TLK model (Chatzipapas et al., 2023).

Parameter	Value	Unit
Starting time point	0	hour
Final time point	336	hour
Time step for integration	0.001	hour
Maximum dose	15	Gy
Constant dose rate	60	$Gy.hour^{-1}$
γ	0.19	-
λ_1	0.1	$hour^{-1}$
λ_2	1	$hour^{-1}$
β_1	0	-
β_2	0.01932	-
η	0.00005	hour-1

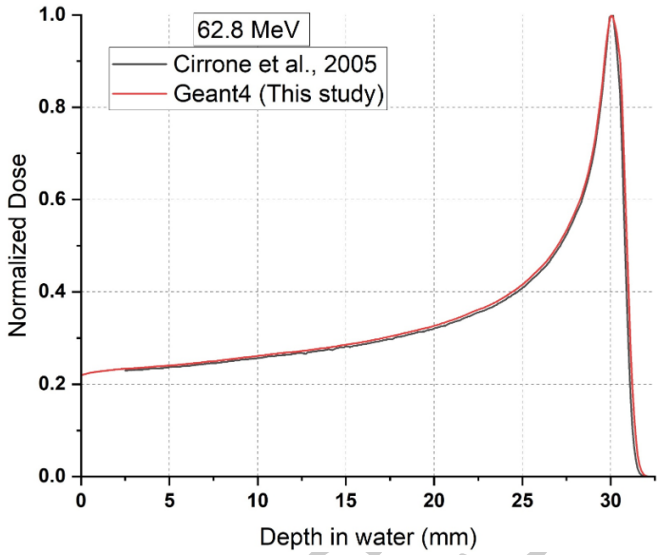

Figure 3: Comparison of Bragg peak curves obtained by Geant4 and the experimental data obtained by ion chamber (Cirrone et al., 2005).

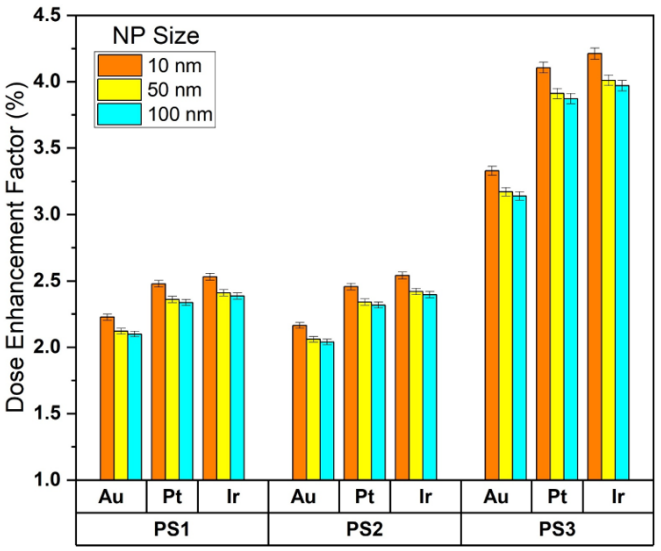

Figure 4: Dose enhancement factor (DEF) which is obtained with 30 $mg.g^{-1}$ Au, Pt, and Ir NPs (with different sizes of 10, 50, and 100 nm) in the fibroblast cell.

To validate the microscopic stage of our simulation, we calculated DSB yields per Gy per Gbp for mono-energetic protons (1-120 MeV) in the absence of NPs and compared them with published data (Belli et al., 2001; Campa et al., 2005; Friedland et al., 2003, 2017). The corresponding LETs for 1, 2, 4, 8, 16, 32, 64, and 128 MeV energies are 29.8, 16.5, 9.56, 5.41, 2.99, 1.61, 0.872, and 0.56 $keV.\mu m^{-1}$, respectively. Table 3 summarizes the results. Our simulated DSB yields agree with literature values within 10% across the tested energy range, confirming the reliability of our Geant4-DNA setup (physics list, DNA geometry, damage scoring criteria) for subsequent NP-enhanced irradiation simulations.

Figure 4 presents the DEF calculated for Au, Pt, and Ir NPs, each at a concentration of 30 $mg.g^{-1}$ and with

Table 3: Double strand break (DSB) yield ($Gy^{-1}Gbp^{-1}$) for 1 to 128 MeV protons.

Energy (MeV)	1	2	4	8	16	32	64	128
This study	12.2	10.1	9.49	8.56	7.87	7.57	7.53	6.91
(Ahmadvand and Kalantari, 2026)	12.2	-	-	-	-	-	-	-
(Friedland et al., 2003)	11.5	9.98	8.58	8.05	7.8	7.51	-	-
(Friedland et al., 2017)	11.75	9.74	8.6	7.85	7.55	7.4	7.325	6.72
(Campa et al., 2005)	11.8	-	-	-	-	-	-	-
(Belli et al., 2001)	13.3	-	-	-	-	-	-	-
Max relative difference (%)	9.02	3.56	9.58	8.29	4.06	2.24	2.72	2.75

diameters of 10, 50, and 100 nm, distributed within the cytoplasm of a fibroblast cell.

Figures 5 and 6 illustrate the enhancement in DNA damage -total SSBs total DSBs, respectively- resulting from the presence of the same set of nanoparticles (Au, Pt, and Ir at 30 $mg.g^{-1}$ and 10, 50, and 100 nm sizes) localized in the cytoplasm.

Figure 7 shows the DSB-to-SSB ratio for each NP type and size under the same conditions, providing insight into the relative complexity of DNA damage induced in the presence of these nanomaterials.

Figure 8 show the ratio of direct to indirect total DNA damages (D_{dir}/D_{ind}) for each NP type and size under the same conditions, providing insight into the relative occurrence of DNA damages induced in the presence of these nanomaterials.

The frequency of irreparable and repairable DSBs per event induced in the cell with and without the presence of 30 $mg.g^{-1}$ Au, Pt, and Ir NPs is shown in Fig. 9.

Figure 10 shows a comparison of the cell survival curves obtained from the TLK model with and without the presence of 30 $mg.g^{-1}$ Pt NPs in the cell cytoplasm. Since the 10 nm size-NPs shows superior DEF as well as DNA damage enhancement, only this size was considered for plotting cell survival curves. The error bars are small and within the marker size. The "H_2O" NP means the condition with no NP present.

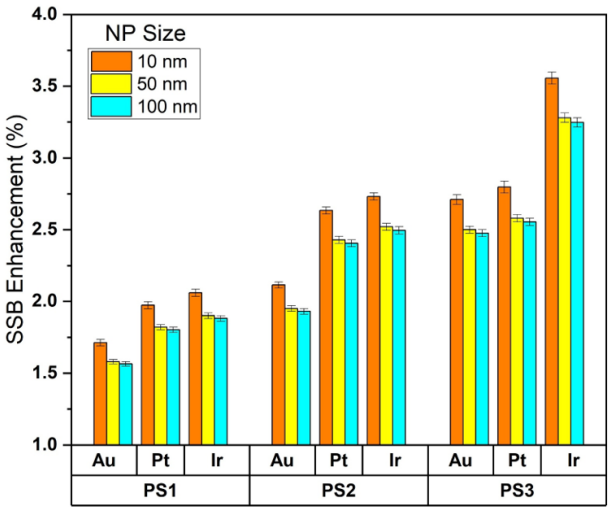

Figure 5: Single DNA strand damage (SSB) enhancement which is obtained with 30 $mg.g^{-1}$ Au, Pt, and Ir NPs (with different sizes of 10, 50, and 100 nm) in the cytoplasm of the cell.

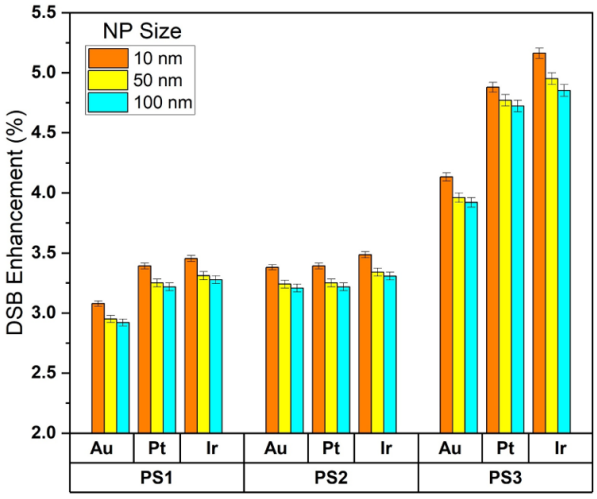

Figure 6: Double DNA strand damage (DSBs) enhancement which is obtained with 30 $mg.g^{-1}$ Au, Pt, and Ir NPs (with different sizes of 10, 50, and 100 nm) in the cytoplasm of the cell.

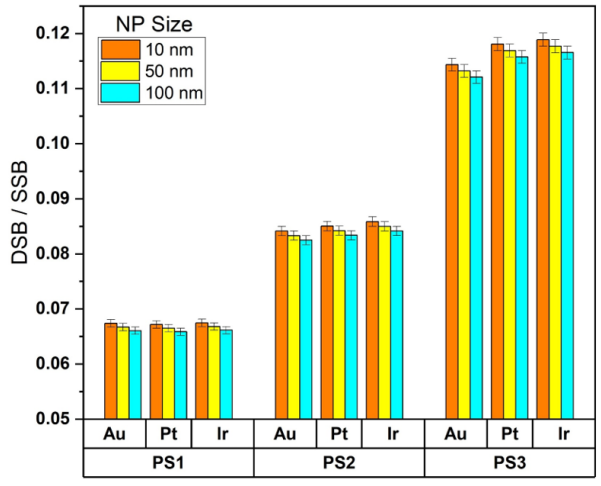

Figure 7: The ratio of DSB/SSB for the presence of 30 $mg.g^{-1}$ Au, Pt, and Ir NPs (with different sizes of 10, 50, and 100 nm) in the cytoplasm of the cell.

4 Discussion

Figure 4 reveals that among the NPs examined, 10 nm Ir nanoparticles yield the highest DEF within the cell, reaching up to 4.21% at position PS3. Pt NPs of the same size exhibit a closely comparable DEF of 4.10%, suggesting similar dose-enhancing behavior, likely attributable to their comparable atomic numbers and densities.

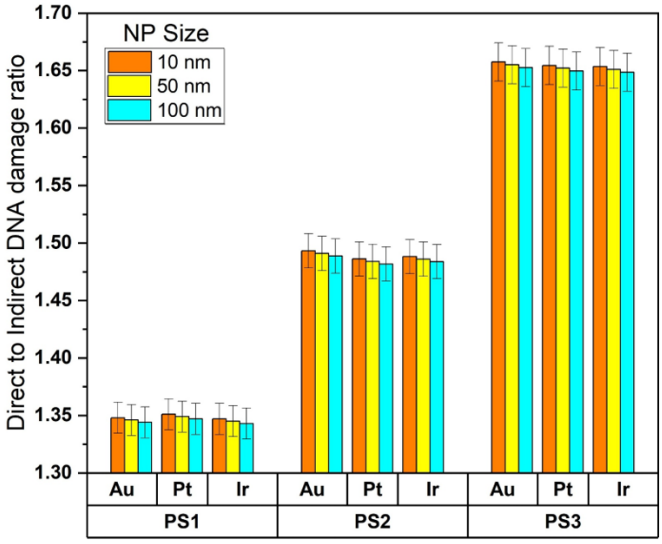

Figure 8: Direct to Indirect DNA damage ratio for the presence of 30 mg.g^{-1} Au, Pt, and Ir NPs (with different sizes of 10, 50, and 100 nm) in the cytoplasm of the cell.

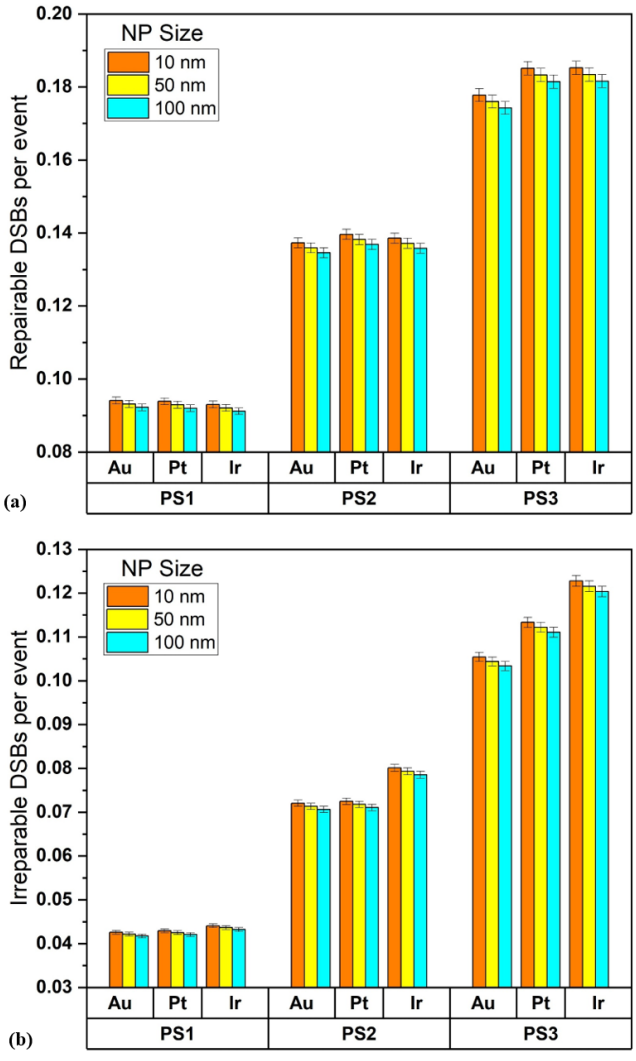

Figure 9: The number of repairable or simle (a) and irreparable or complex (b) DSBs per event induced in the cell nucleus with and without different NPs (30 mg.g^{-1}) with different sizes.

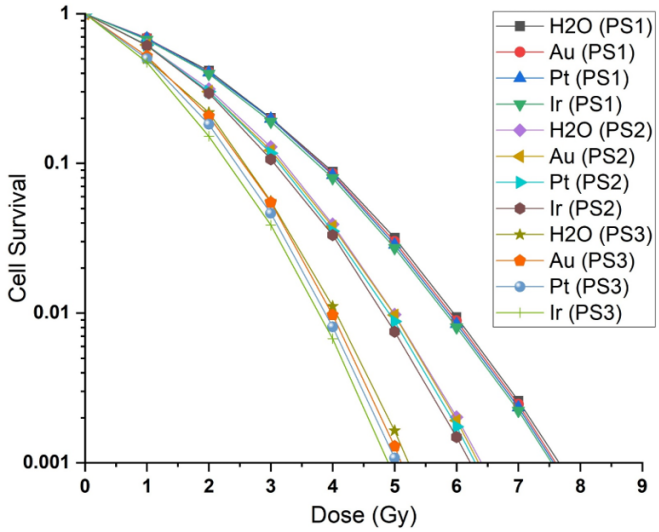

Figure 10: Cell survival curves obtained from the TLK model with and without the presence of 30 mg.g^{-1} Au, Pt, and Ir NPs with 10 nm diameter in the cell. Labels are corresponded to the phase-space locations of the beginning (PS1), the middle (PS2), and the end of SOBP (PS3).

At the beginning (PS1) and middle (PS2) of the proton range, the DEF for Ir and Pt NPs exceeds that of Au NPs by up to 13.7% and 13.5%, respectively. This difference becomes more pronounced at the end of the SOBP (PS3), where Ir and Pt show DEF increases of approximately 26.5% and 23.3% relative to Au. Across all phase-space positions, Ir and Pt consistently demonstrate significantly higher DEF values than Au.

When comparing DEF values along the proton range, all NPs show marked enhancement at the SOBP distal end relative to the entrance region. Specifically, Au, Pt, and Ir exhibit DEF increases of 49.7%, 65.6%, and 62.8%, respectively, at PS3 compared to PS1. Among the three materials evaluated, Au NPs consistently yield the lowest DEF across all positions.

While earlier studies have reported substantial dose enhancement with Au and Ir NPs, the discrepancies between their findings and ours can be attributed to key differences in simulation approaches (McKinnon et al., 2016; Rajabpour et al., 2022; Tabbakh et al., 2022; Mansouri et al., 2024). In those studies, simulations typically involved a single NP directly irradiated by all primary particles, increasing the probability of nuclear interactions and directing secondary particles into a target volume. This target was often modeled as a homogeneous water region without accounting for DNA geometry. Moreover, some studies used mono-energetic proton beams, which do not reflect the SOBP conditions encountered in clinical proton therapy.

In contrast, our simulation aimed to model a more realistic scenario by incorporating the full proton energy spectrum characteristic of the SOBP center, along with a detailed nuclear cell model and a biologically relevant distribution of nanoparticles at a defined concentration within the cytoplasm. This approach yielded a DEF of approximately 3.4% for Au NPs, which aligns with ex-

perimentally reported values. For instance, Smith et al. (Smith et al., 2017) reported a DEF below 5% within experimental uncertainty for 150 MeV protons, while Sisin et al. (Sisin et al., 2022) measured enhancements up to about 9% ± 3% under similar beam conditions. Our simulated result falls comfortably within this experimental range.

The modest residual difference between our simulated 3.4% (for Au NPs) and the upper bound of experimental observations (∼9%) may reflect biological mechanisms not captured by purely physical simulations. These could include biochemical amplification pathways such as sustained catalytic production of reactive oxygen species by nanoparticles or nanoparticle-mediated inhibition of DNA repair processes, both of which could enhance biological effectiveness beyond what would be expected from physical dose enhancement alone.

The modest DEF values reported here (≤4.21%) are consistent with the physical mechanisms of proton energy deposition. Unlike kilovoltage photons, where the photoelectric effect strongly amplifies dose around high-atomic number NPs, protons deposit energy via inelastic collisions that produce secondary electrons with ranges exceeding typical NP dimensions. This dilutes the local enhancement. Nevertheless, the predicted survival fraction reduction at the distal edge (Fig. 10) suggests that even this modest physical enhancement may have biological consequences, particularly if combined with NP-mediated biochemical effects. We also caution that our data cannot definitively separate the effects of density from atomic number, as Ir and Pt have very similar values for both parameters.

McKinnon et al. (McKinnon et al., 2016) reported a 27% dose enhancement for Au NPs using Geant4 simulations. In that study -as in many similar simulation-based investigations- a single NP was modeled, with all primary particles directed to strike it directly, and the dose was scored in ring detectors extending up to 2 μm from the NP center. Other studies employing this same single-NP approach have reported DEFs as high as 1600% for Au and Pt NPs (Mansouri et al., 2024). However, experimental evidence suggests that such dramatic enhancements are not representative of realistic conditions, a discrepancy our simulation results also support.

Our findings align more closely with those of Sotiropoulos et al. (Sotiropoulos et al., 2017), who employed a whole-cell model incorporating Au NPs distributed within the cytoplasm. In their study, irradiation with 10 and 50 MeV protons at a NP concentration of 7 mg.g^{-1} did not yield a significant increase in direct DNA damage. In contrast, as shown in Figs. 5 and 6, the present study observes increases in SSBs ranging from 1.56% to 3.55%, and in DSBs from 2.92% to 5.16%, depending on the phase-space position and NP size.

The primary reason for this difference lies in the scope of damage considered: Sotiropoulos et al. (Sotiropoulos et al., 2017) focused exclusively on direct DNA damage, whereas our simulation accounts for both direct and indirect damage mechanisms, particularly those arising from free radicals generated during water radiolysis. These findings underscore the critical importance of including indirect damage pathways in radiobiological modeling to achieve a more complete understanding of nanoparticle-mediated dose enhancement. The observation that Pt NPs yield a higher DEF than Au NPs at the center of the SOBP and at the other two phase-space positions (as shown in Fig. 4) is consistent with experimental findings reported in the literature (Zwiehoff et al., 2022; Ahmadi Ganjeh and Salehi, 2023). This enhanced performance of Pt over Au- under identical size and concentration conditions -can be attributed to the distinct physicochemical properties of platinum, particularly its greater efficacy in promoting the production of reactive chemical species following irradiation (Zwiehoff et al., 2022).

As the proton beam approaches the distal end of the SOBP, the amount of DNA damage per incident particle increases relative to earlier positions along the beam path. This trend aligns with results from previous studies (Sotiropoulos et al., 2017; Ahmadi Ganjeh et al., 2021) and is explained by the rise in LET near the Bragg peak. The higher LET results in denser ionization events along the proton track, thereby increasing the probability of inducing DNA damage.

However, while our simulations indicate that Ir and Pt NPs yield a higher physical DEF than Au NPs, this does not establish clinical superiority. The final choice of NP for proton therapy is a multi-faceted optimization problem. Au NPs have a more extensive history of biocompatibility and surface functionalization research. Future work must integrate these physical findings with biological data on toxicity, cellular uptake, and potential biochemical radio-enhancing mechanisms to guide the selection of the optimal agent. The observed increase in the DSB-to-SSB ratio with rising LET, as illustrated in Fig. 7, is consistent with the findings reported by Chattaraj and Selvam (Chattaraj and Selvam, 2024). This trend reflects the growing complexity of DNA damage as ionization density increases along the particle track. Moreover, Fig. 8 demonstrates that the ratio of direct-to-indirect DNA damage also increases with LET -corresponding to greater depth in water- which aligns with results from previous studies (Roots et al., 1990; Hirayama et al., 2009; Ito et al., 2006). This behavior underscores the shift in damage mechanism toward a greater contribution of direct energy deposition as LET increases, consistent with the physical characteristics of high-LET radiation.

Figure 9 illustrates that as nanoparticle density increases, the normalized DSB yield per event -comprising both repairable (simple) and irreparable (complex) DSBs- also rises. Accordingly, Ir NPs, with their higher density, produce more DSBs than Pt and Au NPs, explaining the elevated DEF observed with Ir in the cellular environment. Notably, this trend follows nanoparticle density rather than atomic number, suggesting that density may be a more critical parameter than atomic number when selecting NPs for proton therapy applications.

This behavior contrasts with the mechanisms governing low-energy photon interactions, where the photoelectric cross section scales strongly with atomic number. For protons, dose enhancement arises from a different mecha-

nism: protons traversing a high-density, high-atomic number NP have a higher probability of inelastic collisions due to the elevated electron density of the NP material. These collisions generate secondary electrons (δ-rays), a fraction of which escape the NP and deposit dose in the surrounding cellular water. The NP thus acts as a microscopic source of secondary electrons, enhancing local dose. This mechanism scales with NP density because denser materials provide more target electrons per unit volume for proton interactions. Consequently, Ir (ρ = 22.56 g.cm^3) outperforms Au (ρ = 19.32 g.cm^{-3}) under identical conditions. Importantly, this enhancement does not arise from a measurable increase in the bulk density of the tumor (which remains essentially that of soft tissue, ∼1.03 g.cm^{-3} at 30 mg.g^{-1} NP concentration), but rather from localized electron production at the NP-water interface. Furthermore, experimental evidence points to the role of physicochemical properties -such as surface chemistry and catalytic activity- in mediating biological outcomes beyond what physical parameters alone would predict.

An important finding of this study is that as NP diameter increases, both the DEF and DNA damage yields decrease, despite constant mass concentration. This trend arises from two factors. First, smaller NPs are more numerous (see Table 1), increasing the total surface area for proton interactions. Second, and more critically, secondary electrons generated within a NP must escape to deposit dose in the cell. Self-absorption of these electrons scales positively with NP diameter: a 100 nm NP absorbs a larger fraction of its internally generated secondary electrons compared to a 10 nm NP, effectively wasting dose that could otherwise contribute to DNA damage. Consequently, smaller NPs -with lower self-absorption and higher surface area- produce greater localized dose and DNA damage. This inverse relationship is in strong agreement with published results from Rudek et al. (Rudek et al., 2019) and Peukert et al. (Peukert et al., 2020).

DSBs generated from the simulations served as inputs for the TLK mathematical model, from which the cell survival curves presented in Fig. 10 were derived. As illustrated in Fig. 10, at the beginning of the SOBP corresponding to PS1, the survival curves with and without Au, Pt, and Ir NPs show negligible differences. In contrast, at the distal end of the SOBP (PS3), a marked divergence appears between the curves, indicating a significant NP-induced effect. This depth-dependent behavior is closely associated with variations in LET along the proton track.

It should be noted that the specific form of the survival curves is influenced by the choice of mathematical model and the parameter values employed. Nonetheless, the relative difference between NP-containing and NP-free conditions remains a key observation of this study. The observed dependence of survival curve separation on LET -corresponding to different phase-space positions- is consistent with findings reported in related studies (Polf et al., 2011; Jeynes et al., 2014; Li et al., 2016; Zolghadri et al., 2025). Note that for derived quantities (e.g., DSB/SSB ratio, direct/indirect damage ratio), the standard error was propagated using the root-sum-square method. Resulting uncertainties were ≤0.28% and are smaller than the symbol size in all figures (Figs. 4 to 10).

5 Limitations

- High NP concentration: The NP concentration of 30 mg.g^{-1} (3% by weight) used in this study is a theoretical concentration chosen for a controlled, comparative physical simulation, as justified in Section 2.2. It represents an upper bound to elucidate material-dependent effects. Therefore, the absolute DEF values reported here should be interpreted as the maximum theoretical physical enhancement for this concentration. Scaling these results to clinically achievable concentrations requires careful consideration of dose-volume effects and potential nonlinearities.

- Biochemical processes simplification: This study focuses on the physical and radiochemical stages of radiation action (particle transport, radical diffusion). Our model does not incorporate subsequent biochemical enhancement mechanisms that nanoparticles may exhibit, such as catalytic activity sustaining radical production (e.g., Pt NPs acting as nanozymes), interference with DNA repair machinery, or the induction of oxidative stress pathways. These biochemical effects, reported in some experimental studies, could contribute to the overall biological effectiveness beyond the physical dose enhancement quantified here.

- Consideration of biological uptake or aggregation: Our model assumes a homogeneous random distribution of monodisperse nanoparticles within the cytoplasm. Heterogeneous distributions could lead to localized “hot spots” of dose and damage that are not captured by our volume-averaged approach. Furthermore, we did not model a size distribution, which could influence interaction probabilities. Future simulations incorporating more realistic, experimentally-informed biodistribution patterns would be valuable.

- Simulation-based survival curves: The cell survival curves presented are derived entirely from simulation data processed through the TLK model. While the TLK model parameters were taken from literature for fibroblast cells (Chatzipapas et al., 2023), and the trends with LET are consistent with expectations, these curves are predictions that have not been directly validated against experimental clonogenic assays for the specific scenario of NP-enhanced proton irradiation. They serve to illustrate the potential relative biological impact based on the calculated DNA damage spectra. Experimental validation is a crucial next step to confirm the predicted survival modifications.

- Energy range: This study used a single clinically relevant SOBP energy (62.8 MeV). We did not systematically optimize proton energy to maximize DEF.

Our data show that DEF increases with LET (comparing PS1, PS2, and PS3), suggesting that higher LET (lower energy) regions yield greater enhancement. Future work should systematically vary proton energy (e.g., 10-200 MeV) to identify the optimal energy for each NP material.

6 Conclusions

This multiscale simulation study investigated the physical and radiobiological impact of three different NPs with three diameters in a fibroblast cell model irradiated by a clinically relevant 62.8 MeV proton SOBP beam. The results demonstrate that under the simulated conditions, high density NPs like Ir provide a measurable physical dose enhancement of up to 4.21% at a concentration of 30 $mg.g^{-1}$. This enhancement translated into a quantifiable increase in DNA damage complexity and a corresponding reduction in predicted cell survival, particularly at the high-LET distal edge of the SOBP. In contrast, lower density materials produced less physical dose enhancement as well as DNA damages to the cancerous cell.

The primary contributions of this work are threefold: (1) it provides a direct, realistic comparison of NP materials using a clinical SOBP source; (2) it bridges physical dose escalation to radiobiological outcome via DNA damage-based survival modeling; and (3) it underscores that high density NPs like Ir offer a great physical radioenhancement in proton therapy. This suggests that future strategies should consider integrating these physical effects with the biochemical properties of NPs to achieve a more substantial therapeutic gain.

Conflict of Interest

The authors declare no potential conflict of interest regarding the publication of this work.

Funding

The authors declare that no funds, grants, or other financial support were received during the preparation of this manuscript.

References

Agostinelli, S., Allison, J., Amako, K., et al. (2003). Geant4—a simulation toolkit. *Nuclear Instruments and Methods in Physics Research Section A: Accelerators, Spectrometers, Detectors and Associated Equipment*, 506:250–303.

Ahmadi Ganjeh, Z., Eslami-Kalantari, M., Loushab, M. E., et al. (2021). Calculation of direct DNA damages by a new approach for carbon ions and protons using Geant4-DNA. *Radiation Physics and Chemistry*, 179:109249.

Ahmadi Ganjeh, Z. and Mosleh-Shirazi, M. A. (2024). Macroscopic and microscopic investigation of maximum effectiveness of proton-boron capture therapy using Monte Carlo simulation. *Radiation Physics and Chemistry*, 214:111289.

Ahmadi Ganjeh, Z. and Salehi, Z. (2023). Monte Carlo study of nanoparticles effectiveness on the dose enhancement when irradiated by protons. *AIP Advances*, 13(3).

Ahmadvand, Z. and Kalantari, S. Z. (2026). Investigation of relative biological effectiveness for protons, carbon and oxygen ion beams by DNA damage calculations in a fractal fibroblast cell geometry. *Radiological Physics and Technology*, 19(1):243–258.

Ahn, S. H., Lee, N., Choi, C., et al. (2018). Feasibility study of Fe_3O_4/TaO_x nanoparticles as a radiosensitizer for proton therapy. *Physics in Medicine and Biology*, 63(11):114001.

Alamgir, J., Hosseini, S. A., and Salimi, E. (2025). A Monte Carlo study on the impact of a transverse magnetic field on microscopic dose enhancement of nanoparticles in therapeutic proton beams. *Radiation and Environmental Biophysics*.

Allison, J., Amako, K., Apostolakis, J., et al. (2016). Recent developments in Geant4. *Nuclear Instruments and Methods in Physics Research Section A: Accelerators, Spectrometers, Detectors and Associated Equipment*, 835:186–225.

Belli, M., Cherubini, R., Dalla Vecchia, M., et al. (2001). DNA fragmentation in mammalian cells exposed to various light ions. *Advances in Space Research*, 27(2):393–399.

Bertolet, A., Ramos-Méndez, J., McNamara, A., et al. (2022). Impact of DNA Geometry and Scoring on Monte Carlo Track-Structure Simulations of Initial Radiation-Induced Damage. *Radiation Research*, 198(3):207–220.

Campa, A., Ballarini, F., Belli, M., et al. (2005). DNA DSB induced in human cells by charged particles and gamma rays: experimental results and theoretical approaches. *International Journal of Radiation Biology*, 81(11):841–854.

Chattaraj, A. and Selvam, T. P. (2024). Radiation-induced DNA damage by proton, helium and carbon ions in human fibroblast cell: Geant4-DNA and MCDS-based study. *Biomedical Physics & Engineering Express*, 10(4).

Chatzipapas, K. P., Tran, N. H., Dordevic, M., et al. (2023). Simulation of DNA damage using Geant4-DNA: an overview of the molecularDNA example application. *Precision Radiation Oncology*, 7:4–14.

Cirrone, G. A. P., Cuttone, G., Mazzaglia, E. S., et al. (2011). Hadrontherapy: a Geant4-based tool for proton/ion-therapy studies. *Progress in Nuclear Science and Technology*, 2:207–212.

Cirrone, G. P., Cuttone, G., Guatelli, S., et al. (2005). Implementation of a new Monte Carlo-GEANT4 simulation tool for the development of a proton therapy beam line and verification of the related dose distributions. *IEEE Transactions on Nuclear Science*, 52(1):262–265.

Cunningham, C., de Kock, M., Engelbrecht, M., et al. (2021). Radiosensitization Effect of Gold Nanoparticles in Proton Therapy. *Frontiers in Public Health*, 9:699822.

Francis, Z., Villagrasa, C., and Clairand, I. (2011). Simulation of DNA damage clustering after proton irradiation using an adapted DBSCAN algorithm. *Computer Methods and Programs in Biomedicine*, 101(3):265–270.

Friedland, W., Jacob, P., Bernhardt, P., et al. (2003). Simulation of DNA damage after proton irradiation. *Radiation Research*, 159(3):401–410.

Friedland, W., Schmitt, E., Kundrát, P., et al. (2017). Comprehensive track-structure based evaluation of DNA damage by light ions from radiotherapy-relevant energies down to stopping. *Scientific Reports*, 7:45161.

Geant4 Collaboration (2023). *Guide for Physics Lists (for Geant4 version 11.1)*. Accessed: 2023-12-01.

Habibi, F., Parang, Z., Hosseinimotlagh, S. N., et al. (2025). Hadron therapy with nanoparticles for dose enhancement and estimation of DNA damage using GEANT4. *Jordan Journal of Physics*, 18(5):643–658.

Hainfeld, J. F., Dilmanian, F. A., Slatkin, D. N., et al. (2008). Radiotherapy enhancement with gold nanoparticles. *The Journal of Pharmacy and Pharmacology*, 60(8):977–985.

Heuskin, A. C., Gallez, B., Feron, O., et al. (2017). Metallic nanoparticles irradiated by low-energy protons for radiation therapy: Are there significant physical effects to enhance the dose delivery? *Medical Physics*, 44(8):4299–4312.

Hilbert, D. (1935). *Über die stetige Abbildung einer Linie auf ein Flächenstück*. Springer.

Hirayama, R., Ito, A., Tomita, M., et al. (2009). Contributions of direct and indirect actions in cell killing by high-LET radiations. *Radiation Research*, 171(2):212–218.

Hojo, H., Dohmae, T., Hotta, K., et al. (2017). Difference in the relative biological effectiveness and DNA damage repair processes in response to proton beam therapy according to the positions of the spread-out Bragg peak. *Radiation Oncology*, 12(1):111.

Huynh, N. H. and Chow, J. C. (2021). DNA dosimetry with gold nanoparticle irradiated by proton beams: A Monte Carlo study on dose enhancement. *Applied Sciences*, 11(22):10856.

Incerti, S., Baldacchino, G., Bernal, M., et al. (2010a). The Geant4-DNA project. *International Journal of Modeling, Simulation, and Scientific Computing*, 1(02):157–178.

Incerti, S., Ivanchenko, A., Karamitros, M., et al. (2010b). Comparison of Geant4 very low energy cross section models with experimental data in water. *Medical Physics*, 37(9):4692–4708.

Incerti, S., Kyriakou, I., Bernal, M. A., et al. (2018). Geant4-DNA example applications for track structure simulations in liquid water: A report from the Geant4-DNA project. *Medical Physics*, 45(10):e722–e739.

Ito, A., Nakano, H., Kusano, Y., et al. (2006). Contribution of indirect action to radiation-induced mammalian cell inactivation: dependence on photon energy and heavy-ion LET. *Radiation Research*, 165(6):703–712.

Jeynes, J. C., Merchant, M. J., Spindler, A., et al. (2014). Investigation of gold nanoparticle radiosensitization mechanisms using a free radical scavenger and protons of different energies. *Physics in Medicine and Biology*, 59(21):6431–6443.

Jia, S. B., Romano, F., Cirrone, G. A., et al. (2016). Designing a range modulator wheel to spread-out the Bragg peak for a passive proton therapy facility. *Nuclear Instruments and Methods in Physics Research Section A*, 806:101–108.

Karamitros, M., Incerti, S., and Mantero, A. (2011). Modeling radiation chemistry in the Geant4 toolkit. *Progress in Nuclear Science and Technology*, 2:503–508.

Karamitros, M., Luan, S., Bernal, M. A., et al. (2014). Diffusion-controlled reactions modeling in Geant4-DNA. *Journal of Computational Physics*, 274:841–882.

Klapproth, A. P., Schuemann, J., Stangl, S., et al. (2021). Multi-scale Monte Carlo simulations of gold nanoparticle-induced DNA damages for kilovoltage X-ray irradiation in a xenograft mouse model using TOPAS-nBio. *Cancer Nanotechnology*, 12:27.

Kyriakou, I., Sakata, D., Tran, H. N., et al. (2021). Review of the Geant4-DNA simulation toolkit for radiobiological applications at the cellular and DNA level. *Cancers*, 14(1):35.

Lampe, N., Karamitros, M., Breton, V., et al. (2018). Mechanistic DNA damage simulations in Geant4-DNA part 1: A parameter study in a simplified geometry. *Physica Medica*, 48:135–145.

Li, S., Bouchy, S., Penninckx, S., et al. (2019). Antibody-functionalized gold nanoparticles as tumor-targeting radiosensitizers for proton therapy. *Nanomedicine*, 14(3):317–333.

Li, S., Penninckx, S., Karmani, L., et al. (2016). LET-dependent radiosensitization effects of gold nanoparticles for proton irradiation. *Nanotechnology*, 27(45):455101.

Lin, Y., McMahon, S. J., Paganetti, H., et al. (2015). Biological modeling of gold nanoparticle enhanced radiotherapy for proton therapy. *Physics in Medicine and Biology*, 60(10):4149–4168.

Mansouri, E., Almisned, G., Tekin, H. O., et al. (2024). Radiosensitization with metallic nanoparticles under MeV proton beams: local dose enhancement. *Radiation and Environmental Biophysics*.

Martínez-Rovira, I. and Prezado, Y. (2015). Evaluation of the local dose enhancement in the combination of proton therapy and nanoparticles. *Medical Physics*, 42(11):6703–6710.

Martinov, M. P., Fletcher, E. M., and Thomson, R. M. (2023a). Multiscale Monte Carlo simulations of gold nanoparticle dose-enhanced radiotherapy I: Cellular dose enhancement in microscopic models. *Medical Physics*, 50(9):5853–5864.

Martinov, M. P., Fletcher, E. M., and Thomson, R. M. (2023b). Multiscale Monte Carlo simulations of gold nanoparticle dose-enhanced radiotherapy II. Cellular dose enhancement within macroscopic tumor models. *Medical Physics*, 50(9):5842–5852.

McKinnon, S., Guatelli, S., Incerti, S., et al. (2016). Local dose enhancement of proton therapy by ceramic oxide nanoparticles investigated with Geant4 simulations. *Physica Medica*, 32(12):1584–1593.

McNamara, A. L., Kam, W. W., Scales, N., et al. (2016). Dose enhancement effects to the nucleus and mitochondria from gold nanoparticles in the cytosol. *Physics in Medicine and Biology*, 61(16):5993–6010.

Meylan, S., Incerti, S., Karamitros, M., et al. (2017). Simulation of early DNA damage after the irradiation of a fibroblast cell nucleus using Geant4-DNA. *Scientific Reports*, 7(1):11923.

Mohan, R. (2022). A review of proton therapy - current status and future directions. *Precision Radiation Oncology*, 6(2):164–176.

Mortazavi, S. M. J., Rafiepour, P., Mortazavi, S. A. R., et al. (2024). Radium deposition in human brain tissue: A Geant4-DNA Monte Carlo toolkit study. *Zeitschrift für Medizinische Physik*, 34(1):166–174.

Newhauser, W. D. and Zhang, R. (2015). The physics of proton therapy. *Physics in Medicine and Biology*, 60(8):R155–R209.

Nikjoo, H., O'Neill, P., Goodhead, D. T., et al. (1997). Computational modelling of low-energy electron-induced DNA damage by early physical and chemical events. *International Journal of Radiation Biology*, 71(5):467–483.

Peukert, D., Kempson, I., Douglass, M., et al. (2020). Gold nanoparticle enhanced proton therapy: A Monte Carlo simulation of the effects of proton energy, nanoparticle size, coating material, and coating thickness on dose and radiolysis yield. *Medical Physics*, 47(2):651–661.

Plante, I. and Devroye, L. (2017). Considerations for the independent reaction times and step-by-step methods for radiation chemistry simulations. *Radiation Physics and Chemistry*, 139:157–172.

Polf, J. C., Bronk, L. F., Driessen, W. H., et al. (2011). Enhanced relative biological effectiveness of proton radiotherapy in tumor cells with internalized gold nanoparticles. *Applied Physics Letters*, 98(19):193702.

Rajabpour, S., Saberi, H., Rasouli, J., et al. (2022). Comparing Geant4 physics models for proton-induced dose deposition and radiolysis enhancement from a gold nanoparticle. *Scientific Reports*, 12(1):1779.

Ramos-Méndez, J., Shin, W. G., Karamitros, M., et al. (2020). Independent reaction times method in Geant4-DNA: implementation and performance. *Medical Physics*, 47(11):5919–5930.

Roots, R., Holley, W., Chatterjee, A., et al. (1990). The formation of strand breaks in DNA after high-LET irradiation: a comparison of data from in vitro and cellular systems. *International Journal of Radiation Biology*, 58(1):55–69.

Rudek, B., McNamara, A., Ramos-Méndez, J., et al. (2019). Radio-enhancement by gold nanoparticles and their impact on water radiolysis for x-ray, proton and carbon-ion beams. *Physics in Medicine and Biology*, 64(17):175005.

Sakata, D., Belov, O., Bordage, M. C., et al. (2020). Fully integrated Monte Carlo simulation for evaluating radiation induced DNA damage and subsequent repair using Geant4-DNA. *Scientific Reports*, 10(1):20788.

Sakata, D., Lampe, N., Karamitros, M., et al. (2019). Evaluation of early radiation DNA damage in a fractal cell nucleus model using Geant4-DNA. *Physica Medica*, 62:152–157.

Shin, W. G., Sakata, D., Lampe, N., et al. (2021). A Geant4-DNA evaluation of radiation-induced DNA damage on a human fibroblast. *Cancers*, 13(19):4940.

Sisin, N. N. T., Rashid, R. A., Abdullah, R., et al. (2022). Gafchromic^{TM} EBT3 film measurements of dose enhancement effects by metallic nanoparticles for 192Ir brachytherapy, proton, photon and electron radiotherapy. *Radiation*, 2(1):130–148.

Smith, C. L., Best, S. P., Gagliardi, F., et al. (2017). The effects of gold nanoparticles concentrations and beam quality/LET on dose enhancement when irradiated with X-rays and protons using alanine/EPR dosimetry. *Radiation Measurements*, 106:352–356.

Sotiropoulos, M., Taylor, M. J., Henthorn, N. T., et al. (2017). Geant4 interaction model comparison for dose deposition from gold nanoparticles under proton irradiation. *Biomedical Physics Engineering Express*, 3(2):025025.

Stewart, R. D. (2001). Two-lesion kinetic model of double-strand break rejoining and cell killing. *Radiation Research*, 156(4):365–378.

Tabbakh, F. and Hosmane, N. S. (2023). Enhanced biological effectiveness with carbon nanoparticles in proton therapy: a simulation study. *The European Physical Journal Plus*, 138(6):538.

Tabbakh, F., Hosmane, N. S., Tajudin, S. M., et al. (2022). Using Gd-157 doped carbon and Gd-157F4 nanoparticles in proton-targeted therapy for effectiveness enhancement and thermal neutron reduction: a simulation study. *Scientific Reports*, 12(1):17404.

Torrisi, L., Davidkova, M., Havranek, V., et al. (2020). Physical study of proton therapy at CANAM laboratory on medulloblastoma cell lines DAOY. *Radiation Effects and Defects in Solids*, 175(9-10):863–878.

Tran, H. N., Ramos-Méndez, J., Shin, W. G., et al. (2021). Assessment of DNA damage with an adapted independent reaction time approach implemented in Geant4-DNA for the simulation of diffusion-controlled reactions between radio-induced reactive species and a chromatin fiber. *Medical Physics*, 48(2):890–901.

Velten, C. and Tomé, W. A. (2023). Reproducibility study of monte carlo simulations for nanoparticle dose enhancement and biological modeling of cell survival curves. *Biomedical Physics Engineering Express*, 9(4).

Zavestovskaya, I. N., Filimonova, M. V., Popov, A. L., et al. (2024). Bismuth nanoparticles-enhanced proton therapy: Concept and biological assessment. *Materials Today Nano*, 27:100508.

Zavestovskaya, I. N., Popov, A. L., Kolmanovich, D. D., et al. (2023). Boron nanoparticle-enhanced proton therapy for cancer treatment. *Nanomaterials*, 13(15):2167.

Zolghadri, S., Rafiepour, P., and Yousefnia, H. (2025). Quantifying DNA strand breaks from targeted alpha emitters Ac-225 and Th-227 via Geant4-DNA: implications for RBE and cell survival. *EJNMMI Physics*, 12(1):92.

Zwiehoff, S., Johny, J., Behrends, C., et al. (2022). Enhancement of proton therapy efficiency by noble metal nanoparticles is driven by the number and chemical activity of surface atoms. *Small*, 18(9):e2106383.

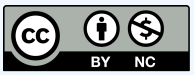

To cite this article:

F. Habibi, Z. Parang, N. Hoseini-Motlagh, Alireza Keshavarz. Proton therapy enhancement with gold, platinum, and iridium nanoparticle: A cellular-scale Geant4-DNA study. *Radiation Physics and Engineering*, In Press.

DOI: 10.22034/rpe.2026.575951.1345

To link to this article: https://doi.org/10.22034/rpe.2026.575951.1345